SCIENTIFIC REPORTS

OPEN

Alkali-created rich properties in grapheme nanoribbons: Chemical bondings

Received: 2 December 2016
Accepted: 21 March 2017
Published online: 11 May 2017

Yu-Tsung Lin[1], Shih-Yang Lin[1], Yu-Huang Chiu[2] & Ming-Fa Lin[1]

The alkali-adsorbed graphene nanoribbons exhibit the feature-rich electronic and magnetic properties. From the first-principles calculations, there are only few adatom-dominated conduction bands, and the other conduction and valence bands are caused by carbon atoms. A lot of free electrons are revealed in the occupied alkali- and carbon-dependent conduction bands. Energy bands are sensitive to the concentration, distribution and kind of adatom and the edge structure, while the total linear free carrier density only relies on the first one. These mainly arise from a single $s - 2p_z$ orbital hybridization in the adatom-carbon bond. Specifically, zigzag systems can present the anti-ferromagnetic ordering across two edges, ferromagnetic ordering along one edge and non-magnetism, being reflected in the edge-localized energy bands with or without spin splitting. The diverse energy dispersions contribute many special peaks in density of states. The critical chemical bonding and the distinct spin configuration could be verified from the experimental measurements.

The graphene-based systems, which are formed by the planar sp^2 bondings of carbon atoms, include layered graphites[1,2], few- and multi-layer graphenes[3,4], one-dimensional graphene nanoribbons (1D GNRs)[5,6] and 1D carbon nanotubes (CNTs)[7,8]. From a geometric point of view, each GNR could be regarded as a finite-width graphene strip or an unzipped CNT. The 1D GNRs have stirred a lot of studies, mainly owing to the complex relations among the honeycomb lattice, the one-atom thickness, the finite-size quantum confinement, and the edge structure. They could be successfully synthesized by the various experimental techniques. The most common methods are to cut graphene, achieved by a metal-catalyzed cutting[9,10], oxidation cutting[11,12], lithographic patterning and etching[13,14], sonochemical breaking[6,15], and molecular precursors[16,17]. The available routes from the unzipping of multi-wall CNTs cover strong chemical reaction[18,19], laser irradiation[20], metal-catalyzed cutting[21,22], plasma etching[23,24], hydrogen treatment and annealing[25], unzipping functionalized CNTs by scanning tunneling microscope (STM) tips[26], electrical unwrapping by transmission electron microscopy (TEM)[27], intercalation and exfoliation[28], and electrochemical unzipping[29]. The other techniques involve chemical vapor deposition[30] and chemical synthesis[31]. GNRs exhibit the feature-rich essential properties, such as, electronic structures[5,32], magnetic properties[32,33], optical spectra[34,35], and transport properties[36,37]. The electronic properties are diversified by changing by the ribbon width (W)[38,39], edge structure[38,40], edge-passivated dopants[41,42], adatom adsorptions[43,44], layer numbers[45], stacking configurations[46], surface curvatures[47,48], mechanical strains[49,50], electric fields[51–53], and magnetic fields[32,54,55]. GNRs are expected to be more potentially applicable in future nanodevices[15,56,57]. In this work, the first-principles calculations are used to investigate the adatom-enriched electronic properties of the alkali-adsorbed GNRs. Whether the alkali adatoms can create the high free electron density will be explored in detail.

GNRs, with or without hydrogen passivation at boundaries, exhibit the semiconducting behavior, as indicated from the theoretical predictions[13,38,39], and the experimental measurements[17,58–60]. There are two typical types of achiral GNRs, namely, armchair and zigzag GNRs. The former have the diverse energy gaps (E_gs) inversely proportional to widths[38,39]. Specifically, E_g in the latter, which arises from the occupied and the unoccupied edge-localized energy bands, is induced by the anti-ferromagnetic spin configuration across the nanoribbon[5,38]. The strong dependence of E_g on W has been confirmed by the electrical conductance[6,13] and tunneling current[17,58–60] measurements. The semiconductor-metal transition is revealed under a transverse electric field[5]. The similar

[1]Department of Physics, National Cheng Kung University, Tainan, 701, Taiwan. [2]Department of Applied Physics, National Pingtung University, Pingtung, 900, Taiwan. Correspondence and requests for materials should be addressed to S.-Y.L. (email: sylin.1985@gmail.com) or M.-F.L. (email: mflin@mail.ncku.edu.tw)

phenomena could also be observed in some edge-decorated GNRs, e.g., Li-, Be-, Na-, K-, transition-metal- and noble-metal-decorated unzipping GNRs[41, 42, 61–63].

There are some theoretical[64–66] and experimental[43, 44] studies on the atom, molecule and polymer adsorptions on the planar GNRs. The first-principles calculations on the Co/Ni-adsorbed GNRs show the spin-split energy bands with the metallic behavior[64]. The adsorption of ligand-protected aluminum clusters on armchair GNRs is predicted to exhibit the semiconducting or metallic band structures, depending on their kinds[65]. The lithium-adsorbed zigzag GNRs can induce the position-dependent spin configurations[66]. Moreover, the polymer-adsorbed GNRs present the effects of the van der Walls interactions on the essential properties[67, 68]. On the experimental side, hydrogen molecules are successfully adsorbed on the Pd-functionalized multi-layer GNRs[43], and tin oxide nanoparticles are synthesized on GNRs to form a composite material[44]. The former and the latter could be utilized as chemical gas sensors and anode materials in lithium ion battery, respectively. However, a systematic theoretical study on the alkali-adsorbed GNRs is absent up to now. The critical orbital hybridization in the alkali-carbon bonds responsible for the creation of conduction electrons, the relations between the free carrier density and the kind, distribution and concentration of adatom, and the dependence of electronic and magnetic properties on the edge structure, width and adatom position are worthy of a detailed examination.

In this paper, the geometric, electronic and magnetic properties of alkali-adsorbed GNRs with various widths are investigated in detail by the first-principles calculations. The ribbon widths, the armchair and zigzag edges, and the kinds, optimal positions, relative distances, single- and double-side adsorptions and concentrations of alkali adatoms, are included in the detailed calculations. There exist the cooperative or competitive relations among the width-dependent quantum confinement, the spin configurations, and the orbital hybridizations in the alkali-carbon bonds. The critical chemical bondings could be analyzed from the atom-dominated energy bands, the spatial charge distribution, and the orbital-projected density of states (DOS). This work shows that they are responsible for the feature-rich electronic properties. All the conduction and valence bands mainly originate from carbon atoms except for few alkali-dominated conduction bands. The high free electron density in the occupied carbon- and alkali-related conduction bands only depends on the adatom concentration. Specifically, the zigzag systems can exhibit three kinds of spin configurations with the distinct edge-localized energy bands, depending on the alkali positions. Moreover, the 1D metallic behavior are clearly evidenced in a high DOS at E_F, accompanied with several prominent peaks. The predicted main features in energy bands and DOS could be examined by angle-resolved photoemission spectroscopy (ARPES) and scanning tunneling spectroscopy (STS), respectively. These rich fundamental features in alkali-adsorbed GNRs are expected to provide potential materials applications in electronic[15, 56] and spintronic[57] devices.

Results

The essential properties of the alkali-adsorbed graphene nanoribbons are investigated for different adatoms, concentrations, distributions, widths, and edge structures. For armchair and zigzag GNRs, their widths are, respectively, characterized by the number of dimer lines and zigzag lines along $\hat{y}$ (N_A and N_Z). The former are chosen for a model study in the alkali-induced free carriers. The optimal adatom position, as shown in Fig. 1(a), is situated at the hollow site, almost independent of the above-mentioned five critical factors. The similar position in 2D graphene has been verified by low-energy electron microscopy[69]. The binding energy of each adatom, the reduced energy due to alkali adsorption, is characterized as $E_b = (E_{sys} - E_{gra} - nE_A)/n$, where E_{sys}, E_{gra} and E_A are the total energies of the alkali-adsorbed system, the graphene sheet, and the isolated alkali atom, respectively. Li and Na adatoms, respectively, have the largest and smallest binding energies (-0.75 eV and -0.23 eV in Table 1). The adatom height strongly depends on the atomic number, in which h_{ad} varies from 1.75 Å to 3.06 Å as Li → Cs. Also, the alkali-carbon (A-C) bond lengths grow with the radius of adatom, ranging from 2.23 Å to 3.37 Å. These clearly illustrate that Li adatoms have the strongest bondings with carbon atoms among the alkali-adsorbed systems. GNRs remain the planar structure so that the σ bonding due to ($2s$, $2p_x$, $2p_y$) orbitals of carbon atoms is almost unchanged after alkali adsorption. However, the C-C bond lengths are sensitive to the positions of carbon atoms, but not those of alkali adatoms. In addition, the total ground state energy only presents a negligible change (about several meVs) during the variation of adatom position.

Electronic structures of GNRs are dramatically changed by the alkali-atom adsorption, especially for free electrons in conduction bands. Pristine armchair nanoribbons exhibit a lot of 1D energy bands, as shown in Fig. 2(a) for the $N_A = 12$ armchair GNR. Most of them belong to parabolic bands, while few of them have partially flat dispersions within a certain range of k_x (e.g., $E^v = -2.1$ eV, -4.7 eV; -5.7 eV). All the energy dispersions present the monotonous k_x-dependence except for the subband anti-crossings. The occupied valence bands are asymmetric to the unoccupied conduction bands about the Fermi level ($E_F = 0$). There is a direct energy gap of $E_g = 0.61$ eV at the Γ point, mainly owing to the effect of quantum confinement. The electronic states, with $|E^{c,v}| \le 2$ eV, come from the π bondings of the parallel $2p_z$ orbitals, and the others are closely related to the σ bondings of ($2s$, $2p_x$, $2p_y$) orbitals. In general, the band-edge states occur at $k_x = 0$ and 1 (in unit of $\pi/3b$). Such critical points are also revealed at other k_x's in the presence of subband anti-crossings.

The alkali-adsorbed graphene nanoribbons exhibit the similar band structures, as clearly indicated in Fig. 2(b–f). The conduction bands are easily modulated by the alkali adatoms. The energy dispersions of valence states are changed by the adatom adsorption, while their number and the dominance of carbon atoms keep the same. These are mainly determined by the orbital hybridizations in A-C bonds bonds (discussed later in Fig. 5). The Fermi level (E_F) is changed from the middle of energy gap into the conduction bands, directly reflecting the high charge transfer from alkali atoms to adsorbed systems. The Fermi momentum can characterize the linear free carrier density arising from each occupied conduction band by the relation $\lambda = 2k_F/\pi$. There are some extra conduction bands which are created by the alkali adatom. Specifically, there are two or three conduction bands intersecting with the E_F, depending the kinds of alkali adatoms. The lowest and/or highest ones are dominated by carbon atoms, and another one by adatoms (dominance proportional to the radius of green circle). The adatom-induced

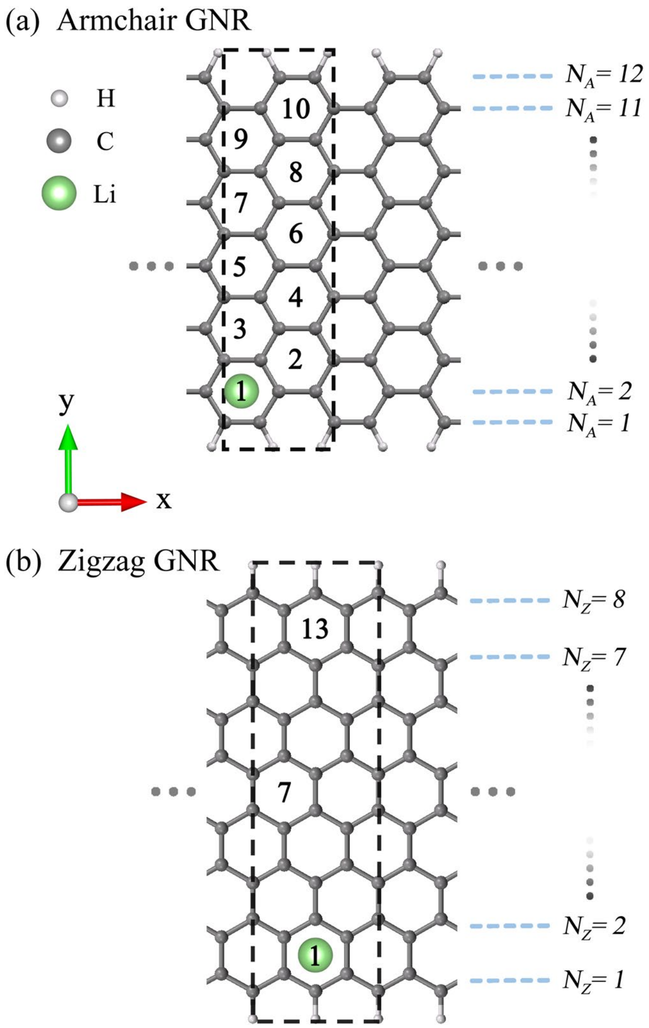

Figure 1. Geometric structures of alkali-adsorbed GNRs for (**a**) $N_A = 12$ armchair and (**b**) $N_Z = 8$ zigzag systems. The dashed rectangles represent unit cells used in the calculations. The lattice constants are, respectively, $a = 3b$ and $a = 2\sqrt{3}\,b$ for armchair and zigzag GNRs. Numbers inside hexagons denote the adatom adsorption positions.

$N_A = 12$	E_b (eV)	nearest C-C (Å)	bond length A-C (Å)	height (Å)	λ (10^7 e/cm)	λ/adatom concentration (e)	Bader charge transfer (e)
Li	−0.75	1.384	2.23	1.75	2.31	0.995	0.75
Na	−0.23	1.377	2.27	2.46	2.35	1.011	0.44
K	−0.39	1.375	3.21	2.81	2.31	0.995	0.45
Rb	−0.68	1.374	3.36	2.96	2.36	1.013	0.47
Cs	−0.59	1.374	3.37	3.06	2.31	0.995	0.54

Table 1. Binding energies, bond lengths, heights, and free electron densities of $N_A = 12$ alkali-adsorbed GNRs with one adatom in a unit cell.

conduction bands are quite different among the various alkali systems, but the distinct systems possess the almost same free electron density (discussed in Table 1). In addition, energy bands almost keep the same during the variation of the single-adatom position (not shown).

The electronic structures are enriched by the concentration, relative position, single- and double-side adsorption, and edge structure. When two Li adatoms are situated at the distinct edges of the same side, there are five conduction bands with free electrons, as shown in Fig. 3(a). They only make important contributions for two low-lying conduction bands. The relative position can drastically alter conduction bands near E_F. For two neighboring adatoms ($(3, 7)_{single}$ in Fig. 1), only one Li-dominated conduction band has free carriers, while another higher-energy one is fully unoccupied (Fig. 3(b)). It should be noticed that the total sum of the Fermi momenta

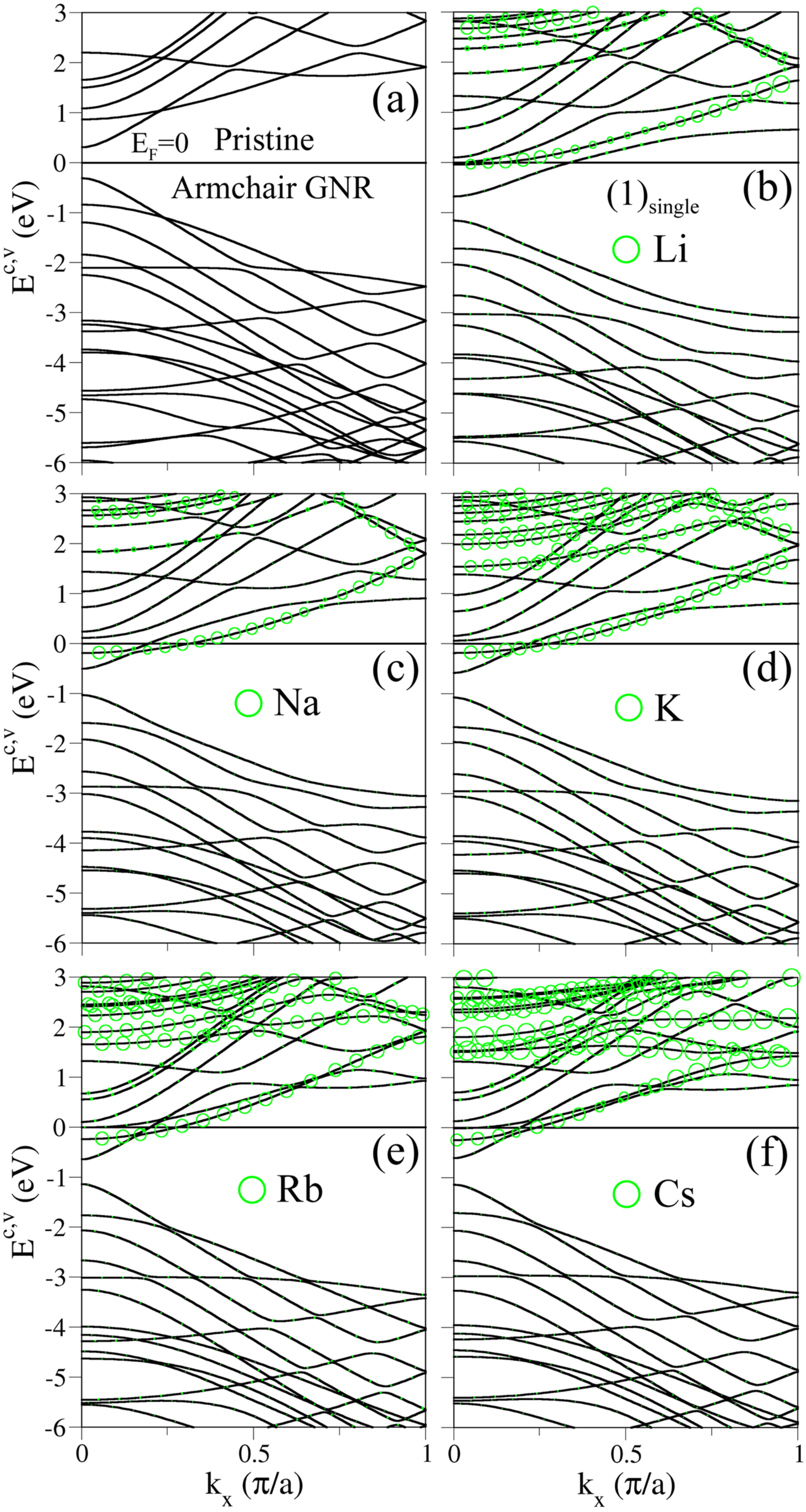

Figure 2. Band structures of $N_A = 12$ armchair systems for (**a**) a pristine GNR, and the (**b**) Li-, (**c**) Na-, (**d**) K-, (**e**) Rb- and (**f**) Cs-adsorbed GNRs with an adtom at edge. Green circles represent the contributions of alkali adatoms.

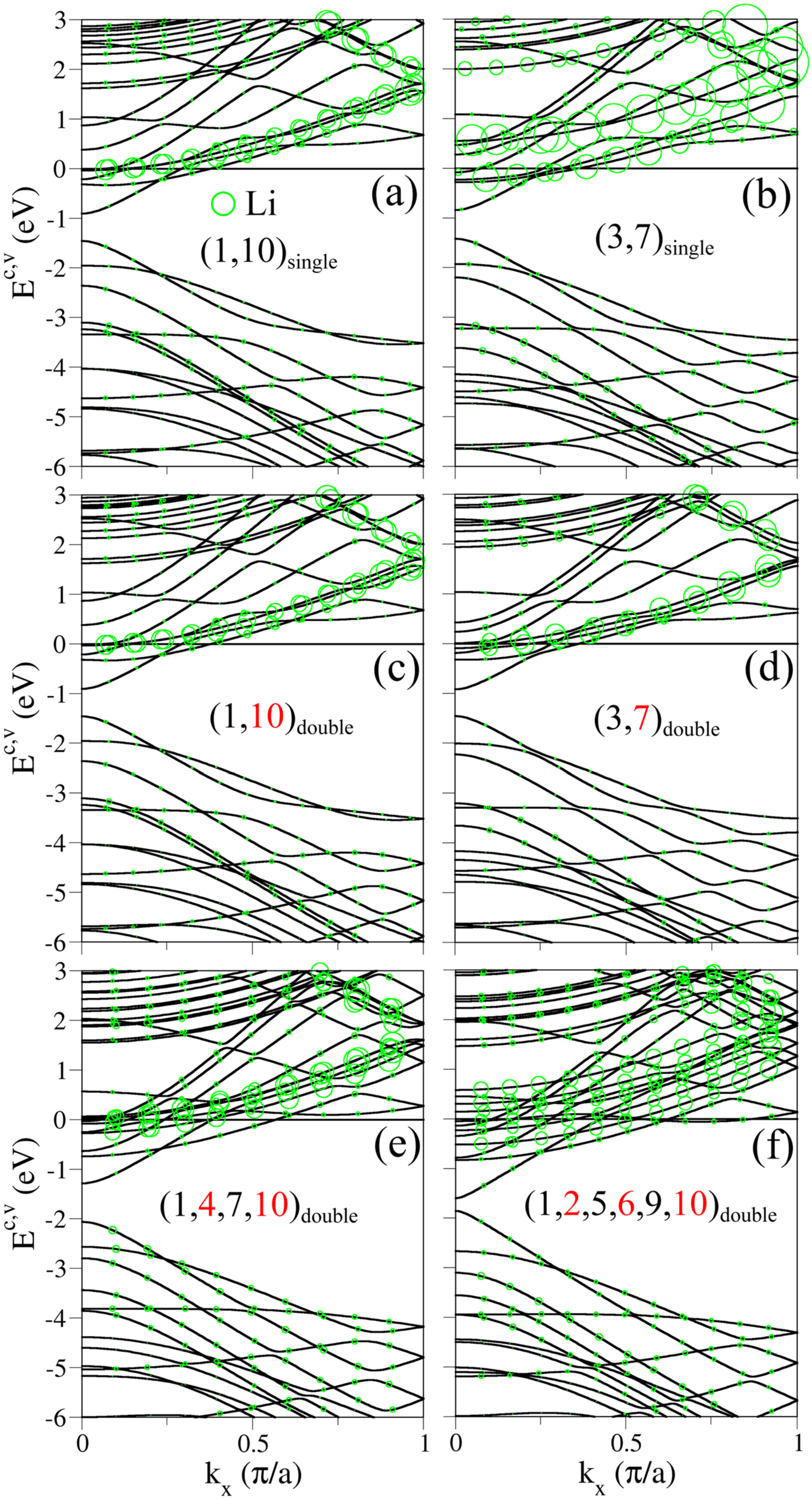

Figure 3. Similar plot as Fig. 2, but shown for the Li-adsorbed GNRs. (**a**,**b**), respectively, correspond to the single-side adsorptions of adatoms at $(1, 10)_{single}$ and $(3, 7)_{single}$. The double-side adsorptions are shown for two adtoms at (**c**) $(1, 10)_{double}$ & (**d**) $(3, 7)_{double}$, four adatoms at $(1, 4, 7, 10)_{double}$, and six adatoms at $(1, 2, 5, 6, 9, 10)_{double}$. Numbers correspond to the adatom adsorption position. Two colors (black & red) denote two distinct sides.

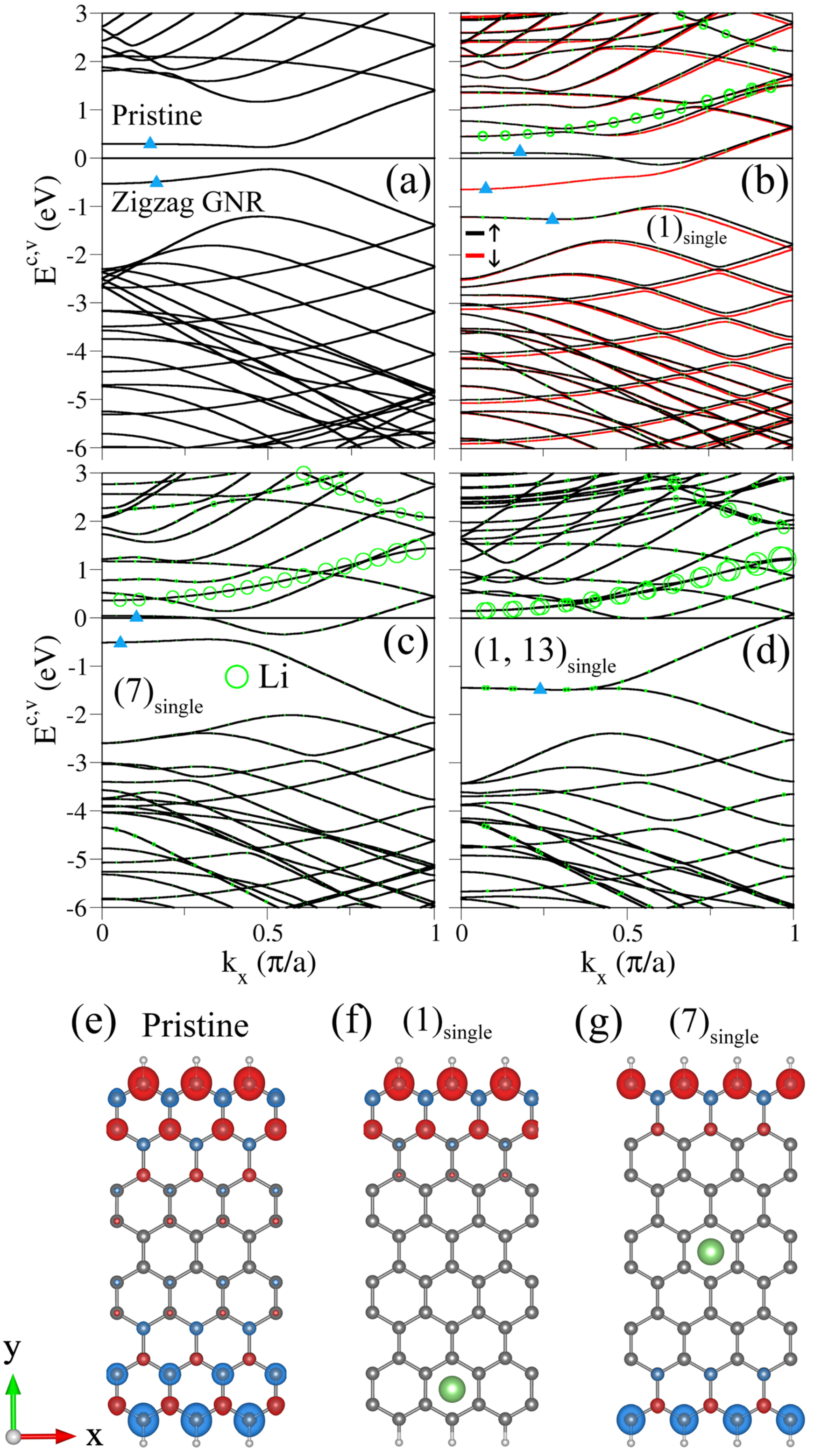

Figure 4. Band structures of $N_Z = 8$ zigzag systems for (**a**) a pristine GNR and the Li adsorptions situated at (**b**) a single edge, (**c**) a ribbon center and (**d**) two edges of single side. The spin configurations of (**a**–**c**) are indicated in (**e**–**g**), respectively. Blue and red circles, respectively, represent spin-up and spin-down arrangements.

is hardly affected by the relative position. This clearly indicates that the interactions between two alkali adatoms are not responsible for the free carrier density. As to the variation from the single- to double-side absorptions, the conduction bands present an obvious change except for the two-adatom case with the sufficiently long distance. For example, bands structures are different from each other in the single- and double-side adsorptions with two

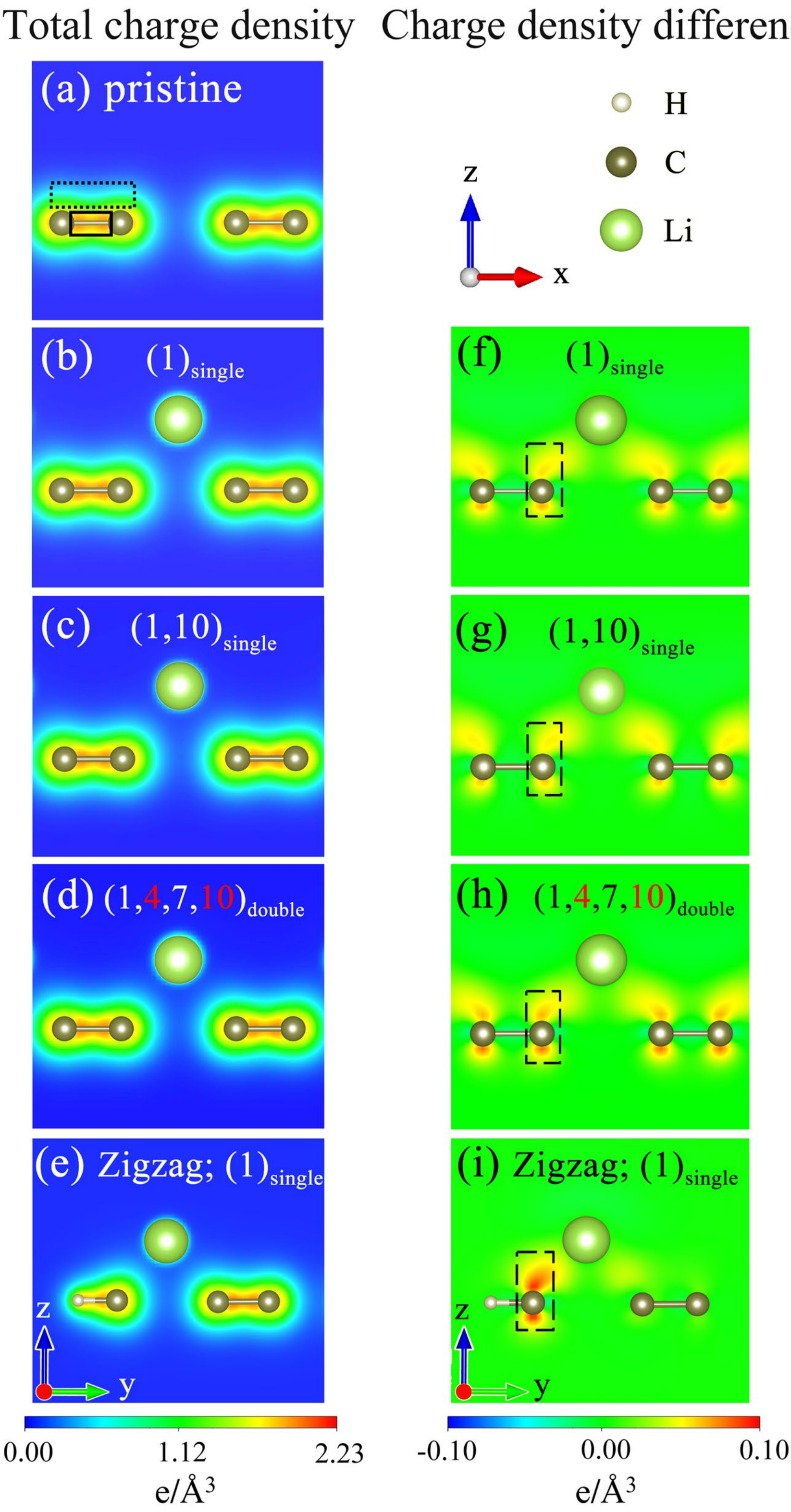

Figure 5. The spatial charge distributions of $N_A = 12$ armchair systems for (**a**) a pristine GNR, (**b**) an adatom at edge $(1)_{single}$, (**c**) two adatoms at $(1, 10)_{single}$ and (**d**) four adatoms at $(1, 4, 7, 10)_{double}$. The π and σ bondings are, respectively, enclosed by the dashed and solid rectangles. The charge density differences, corresponding to (**b**–**d**), are revealed in (**f**–**h**), respectively. Also shown in (**e**) and (**i**) are those of $N_z = 8$ zigzag system with an adatom.

GNR systems	configurations	λ (10^7 *e/cm*)	λ/adatom concentration (e)	Bader charge transfer (e)
Armchair $N_A = 12$	$(3, 7)_{single}$	4.67	1.008	0.69
	$(3, 7)_{double}$	4.62	0.989	0.75
	$(1, 10)_{single}$	4.68	1.008	0.74
	$(1, 10)_{double}$	4.67	1.008	0.74
	$(1, 4, 7, 10)_{double}$	9.24	0.994	0.71
	$(1, 2, 5, 6, 9, 10)_{double}$	13.96	1.007	0.70
Zigzag $N_Z = 8$	$(1)_{single}$	2.02	1.001	0.88
	$(7)_{single}$	2.03	1.009	0.89
	$(1, 13)_{single}$	4.10	1.015	0.88
	$(1, 13)_{double}$	4.02	1.001	0.88

Table 2. Free electron densities for various numbers and positions of adatoms in $N_A = 12$ and $N_z = 8$ alkali-adsorbed GNRs.

adatoms close to the ribbon middle (Fig. 3(b,d)), and the opposite is true for the long-distance case (Fig. 3(a,c)). With the increasing concentration, there are more free carriers in the alkali-created and carbon-dependent conduction bands, as revealed in Fig. 3(e,f). In addition, the adatom dominance on the valence bands gradually grows, mainly owing to more C-alkali interactions (the increased radii of green circles).

The edge structure can dramatically change the electronic structures in the absence and presence of adatom adsorption. Zigzag GNRs are in sharp contrast with armchair GNRs. The former possess the anti-ferromagnetic ordering across the nanoribbon and the ferromagnetic configuration at each zigzag edge, as clearly illustrated in Fig. 4(e). Zigzag GNRs present a pair of partially flat energy bands nearest to E_F (blue triangles in Fig. 4(a)), in which their wavefunctions are localized at edge boundaries[38]. That is, such energy bands mainly come from the edge carbon atoms. Their energy dispersions become strong at large k_x's, in which the extra band-edge states come to exist there. The similar states are also revealed in alkali-adsorbed zigzag GNRs (Fig. 4(b,c)). Both partially flat energy dispersions and band-edge states are expected to induce the distinct special structures in DOS. Furthermore, they can create a direct energy gap at $k_x = 0.5$ in the anti-ferromagnetic configuration, e.g., $E_g = 0.46$ eV for a $N_Z = 8$ ZGNR. It should be noticed that energy gap is determined by the strong competition between spin configuration and quantum confinement. The energy bands are doubly degenerate in the spin degree of freedom, independent of the spin-up- and spin-down-dominated configurations.

Band structures and spin configurations are very sensitive to the changes in the distribution and concentration of adatom. When one alkali adatom is located near the zigzag edge (Fig. 4(b)), the spin-degenerate electronic states become split. The two edge-localized energy bands, which intersect with the Fermi level, have an obvious splitting of ~0.7 eV. However, another two ones below E_F only exhibit a weak splitting. The former and the latter are, respectively, dominated by edge carbon atoms away from and near adatoms. These clearly indicate that the spin configurations are strongly suppressed by the A-C interactions, as revealed from Fig. 4(f). There exists the ferromagnetic ordering at one edge without adatoms. This is responsible for the spin-split energy bands which present more free carriers in the spin-down conduction band (the red curve crossing E_F). On the other hand, the spin degeneracy and the anti-ferromagnetic configuration are recovered, while the adatoms are situated at the ribbon center. The absence of spin distributions near adatoms, as shown in Fig. 4(g), further illustrates the magnetic suppression. According to the above-mentioned specific relation between spin distribution and adatom position, the spin-dependent properties are identified to be disappeared for two adatoms at distinct edges, e.g., the spin-degenerate energy bands without magnetism in Fig. 4(d). Furthermore, the two edge-localized energy bands are merged together at $E^v = -1.35$ eV for $|k_x| \leq 0.5$. In addition, the typical magnetic momenta of the edge carbon atoms are about 0.10~0.15 μ_B under the ferromagnetic ordering along the zigzag edge. In short, three kinds of magnetic configurations in alkali-adsorbed zigzag GNRs, the anti-ferromagnetic ordering across the ribbon, ferromagnetic ordering only along one edge and non-magnetism, are mainly determined by the adatom positions. Specifically, the second kind of spin configuration corresponds to the spin-split energy bands with the different free electron densities. Such electrons under transport measurements are expected to create the spin-polarized currents, indicating potential applications in spintronic devices[57]. In addition, the spin-dependent configurations in 2D graphene could be induced by the transition metal adatoms[70].

The adatom-induced linear free electron density deserves a closer examination. By the detailed analyses and calculations, the total carrier density in conduction bands below E_F is just equal to the adatom density in a unit cell. This is independent of the kinds of adatoms, the adatom positions, the single- or double-side adsorptions, the edge structures, and the ribbon widths, as clearly revealed in Tables 1 and 2. These indicate that the orbital hybridizations in alkali-C bonds (or the π bondings in Fig. 5) are almost the same under various adatom adsorptions. The alkali-created free electron density is estimated to be about $\lambda \sim 2.31 - 2.37 \times 10^7$ e/cm for a single adatom in an armchair unit cell, and it can reach $\lambda \sim 1.40 \times 10^8$ e/cm for the double-side adsorption of six adatoms in $N_A = 12$ armchair GNR. Specifically, the alkali adatoms are deduced to contribute the outmost s-orbital electrons as free carriers in adsorbed systems. The similar results could be generalized to alkali-adsorbed 2D graphenes, i.e., the 2D electron density is dominated by the adatom density, but not the distribution configurations. On the other hand, the charge transfer between alkali and carbon atoms could also be obtained from the Bader analysis. However, it is sensitive to the changes in the kind, position and concentration of adatom, directly reflecting that this analysis cannot be utilized to evaluate the free carrier density in adatom-adsorbed GNRs. The free electron density could be greatly enhanced by the increase of adatom concentration, so that the electrical conductance is expected to behave so. The alkali-doped GNRs might be promising materials in nanoelectronic devices[15, 56] or next-generation supercapacitors, e.g., the ultrafast rechargeable metal-ion battery[71, 72], and the large reversible lithium storages[73, 74].

Recently, ARPES has emerged as the most powerful experimental technique in the identification of the wave-vector-dependent electronic structures. The experimental measurements on the graphene-related systems could be used to explore the feature-rich band structures under the different dimensions[75–83], the various stacking configurations[77–81], and the distinct adatom adsorptions[82, 83]. The AB-stacked graphite exhibits the 3D π energy bands, with the bilayer and monolayer-like energy dispersions, respectivily, at $k_x = 0$ and zone boundary of $k_x = 1$ (K and H points in the 3D first Brillouin zone)[75, 76]. The verified electronic structures of 2D few-layer graphenes include the Dirac-cone structure in single-layer system[77–79], two pairs of parabolic bands in bilayer AB stacking[77, 80], the linear and parabolic bands in tri-layer ABA stacking[77, 81], the partially flat, sombrero-shaped and linear bands in tri-layer ABC stacking[81], the red-shift Dirac cone in alkali-adsorbed graphenes[82], and the gap opening in graphene oxides[83]. The 1D parabolic energy bands in graphene nanoribbons have been directly observed[16]. Up to now, the ARPES measurements on the unusual energy bands in alkali-adsorbed GNRs are absent. The further examinations are required for the occupied valence and conduction bands near the Fermi level, including the alkali-dominated conduction bands, the carbon-related conduction and valence bands, and the distribution-, concentration- and edge-dependent ones. They are useful in understanding the single $s-2p_z$ orbital hybridization in the alkali-C bond. Specifically, the experimental verifications on the existence of Fermi momenta or energy gap and the spin degeneracy of edge-localized energy bands can identify the spin configurations in zigzag GNRs.

The orbital hybridizations in chemical bondings, which are responsible for the rich electronic properties, are clearly evidenced by the spatial charge distributions. They could be characterized by the carrier density (ρ) and the difference of carrier density ($\Delta\rho$). The latter is created by subtracting the pristine system from that of the adatom-adsorbed one. For a planar graphene nanoribbons, the parallel $2p_z$ orbitals and the planar ($2s$; $2p_x$; $2p_y$) orbitals can form the π bondings and the σ bondings, respectively, as shown by the dashed and the solid rectangles in Fig. 5(a). The σ orbital hybridizations, with very high charge density between two carbon atoms, belong to covalent bonds. They keep the same under the alkali adatom adsorptions, corresponding to the zero $\Delta\rho$ in Fig. 5(f–i). Also, the π bondings could survive in alkali-adsorbed graphenes for any concentrations, distributions and edge structures, as illustrated in Fig. 5(b–e). However, the modifications on them are observable through the charge variations between alkali and carbon atoms (the dashed rectangles in Fig. 5(f–i)). Also shown is that $\Delta\rho$ is absent in neighboring carbon atoms, or the planar σ bonding remains the same after alkali adsorption. These indicate that there only exist a single $s-2p_z$ orbital hybridization in the A-C bond.

DOS can exhibit many special structures due to the band-edge states in 1D energy dispersions, as clearly indicated in Fig. 6(a–h). The asymmetric and symmetric peaks are, respectively, presented in the square-root and delta-function-like divergent forms, being associated with the parabolic and partially flat energy dispersions. Their intensities are proportional to the inverse of curvature and the dispersionless k_x-range. For a pristine armchair GNR, an energy gap, with zero DOS, is revealed between one pair of opposite-side anti-symmetric peaks (Fig. 6(a)). It almost keeps the same after alkali adsorption, but changes into an energy spacing between valence and conduction bands. The prominent peaks within $|E| \leq 3$ eV are dominated by $2p_z$ orbitals (red curve) and those of $E < -3$ eV by $2p_x + 2p_y$ orbitals (green curve). There are minor modifications on the carbon-dependent peak structures under the alkali adsorption (Fig. 6(a,b)), i.e., a red shift of DOS could be observed from the change of E_F. Specifically, the adatoms can create pronounced asymmetric peaks near E_F, corresponding to the alkali-dominated occupied or unoccupied conduction bands. The energy and number of special structures depend on the distribution and concentration (Fig. 6(c,d)). Such peaks might merge with the carbon-dependent ones. The main differences between zigzag and armchair GNRs lie in the low-lying peak structures. The former can present the delta-function-like symmetric structures arising from the edge-localized energy bands, being sensitive to the spin configurations. The anti-ferromagnetic, ferromagnetic and non-magnetic zigzag GNRs, respectively, possess a pair of symmetric peaks (blue triangles in Fig. 6(e,g)), three peaks (Fig. 6(f)), and a merged peak (Fig. 6(h)). The peak intensities are obviously reduced for the spin-split energy bands (a pair of symmetric peaks across $E = 0$ in Fig. 6(f)).

The STS measurements, in which the differential tunneling conductance (dI/dV) is approximately proportional to DOS and directly reflects its special structures, could serve as an efficient way to confirm the contributions of carbon and alkali atoms. They have been successfully utilized to verify the diverse electronic properties in graphite[84], few-layer graphenes[85–88], carbon nanotubes[89, 90], and GNRs[17, 58–60]. The experimental identifications include the splitting π and π^* peaks at middle energy of $|E| \sim 2$ eV and a finite DOS at E_F in semi-metallic AB-stacked graphite, a V-shaped spectrum vanishing at the Dirac point in monolayer graphene[85], the asymmetry-created peak structures in bilayer graphene[86–88], and the geometry-dependent energy gaps and the asymmetric peaks of 1D parabolic bands in carbon nanotubes and GNRs. The main features of electronic properties, including the energy spacing between valence and conduction bands, the alkali-dominated special structures close to E_F, a lot of carbon-induced asymmetric peaks at a whole energy range, and the prominent symmetric peaks of partially flat edge-localized bands with or without spin splitting could be further investigated with STS. The STS measurements on the low- and middle-energy peak structures are useful in identifying the single-orbital bonding and the specific spin configurations in alkali-adsorbed GNRs.

Discussion

The geometric structures, electronic and magnetic properties of alkali-adsorbed GNRs are studied using the first-principles calculations. They are shown to be, respectively, determined by the adatom position, a single

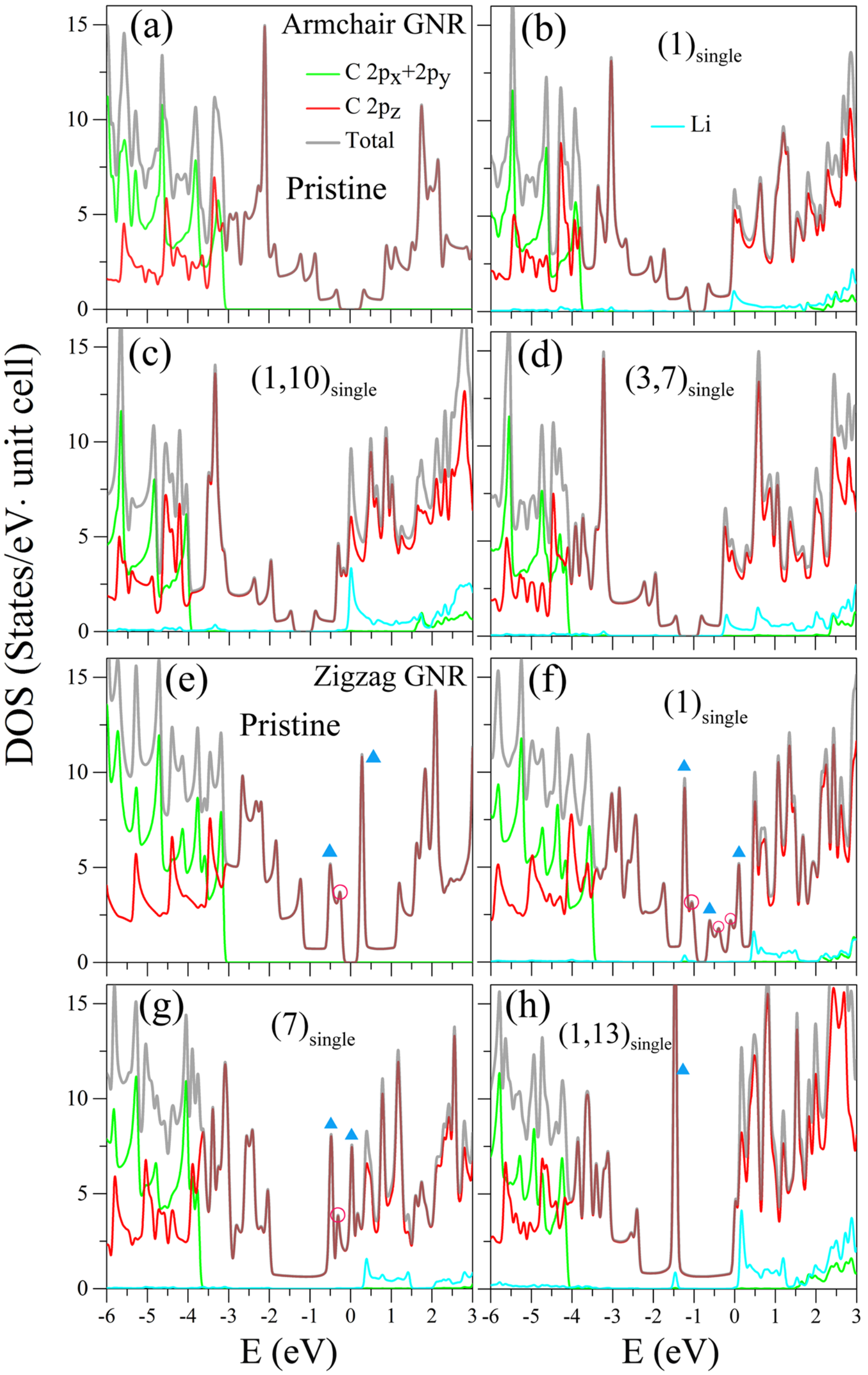

Figure 6. The total and orbital-projected DOSs of $N_A = 12$ armchair systems for (**a**) a pristine GNR, (**b**) an adatom at edge $(1)_{single}$, and the double-side adsorptions of (**c**) two adatoms at $(1, 10)_{single}$ and (**d**) $(3, 7)_{single}$. Those of $N_Z = 8$ zigzag systems are shown for (**e**) a pristine GNR, and the Li adsorptions situated at (**f**) $(1)_{single}$, (**g**) a ribbon center $(7)_{single}$ and (**h**) two edges $(1, 13)_{single}$.

$s - 2p_z$ orbital hybridization in A-C bond, and the spin configurations at two edges. The critical chemical bonding is responsible for the feature-rich electronic properties, including the occupied carbon- and alkali-dominated conduction bands near E_F, and a linear relation between the linear free electron density and the adatom concentration. Any alkali atoms contribute the outmost s orbitals to become free carriers in adsorbed systems. The creation of high free carrier density indicates that alkali-adsorbed GNRs might have potential applications in nanoelectronic devices[15, 56]. Moreover, the single-edge adsorption causes ZGNRs to exhibit the spin-split metallic energy bands. They could be considered as promising materials for future applications in spintronic devices[57].

The essential properties are diversified by the cooperative or competitive relations among quantum confinement, A-C interaction, and spin configuration. GNRs keep a planar structure after alkali adsorption, indicating the unchanged σ bondings of carbon atoms. The optimal position of adatom is located at the hollow site, in which its height grows with the atomic number. The predicted geometric structure could be verified by the STM measurements[89, 90]. GNRs change from semiconductors to metals during the gradual increase of adsorption concentration. The alkali-adsorbed GNRs possess the well-extended π bonding, while there exist charge variations between alkali and carbon atoms. The former is the main reason for the minor modifications on the carbon-dominated valence bands. The latter arises from the $s-2p_z$ hybridization so that the alkali- and carbon-dependent conduction bands rely on the kind, distribution, and concentration of adatom. Also, the edge structure plays a critical role in magnetic and electronic properties. Zigzag systems can present the anti-ferromagnetic ordering between two edges, the ferromagnetic configuration only at one edge, or the non-magnetism, depending on whether adatoms are close to the boundaries. They have the partially flat edge-localized energy bands near E_F; furthermore, both spin-up and spin-down states are split under the single-edge adsorption. The distinct free carrier density in the splitting energy bands could create the spin-polarized current in transport measurements. The ARPES measurements[75–83] are suitable for the identification of diverse energy bands. The 1D energy dispersions are directly reflected in DOS as a lot of special structures. The anti-symmetric and symmetric peaks, respectively, correspond to the parabolic and partially flat energy bands. The STS measurements on the alkali-dominated anti-symmetric peaks near E_F could be utilized to examine the critical chemical bonding. The distinct spin configurations in alkali-adsorbed zigzag GNRs are distinguishable by measuring the number, energy, and intensity of low-lying symmetric peaks.

This work shows that the first-principles calculations, combined with the critical orbital hybridizations in adatom-carbon and carbon-carbon bonds and the specific spin arrangements, are useful in exploring the orbital- and spin-dominated essential properties. For example, band structure, free carrier density, and DOS are determined by which kinds of atomic orbitals and spin configurations These could be further generalized to the layered condensed-matter systems, with the nano-scaled thickness and the unique lattice symmetries. In addition to graphene, the emergent layered materials include silicene, germanene, tinene, phosphorene, MoS_2 and so on. Whether the alkali adsorptions on these semiconducting nanoribbon systems can create the high free carrier density deserves a thorough and systematic study. The complicated relations among quantum confinement, geometric symmetry, multi-orbital hybridizations in chemical bonds, and spin-orbital interactions, being responsible for the essential properties, need to be investigated in detail.

Methods

The first-principles calculations on the geometric and electronic properties of graphene nanoribbons are performed by using Vienna *ab initio* simulation package[91]. The exchange-correlation energy of interacting electrons is evaluated from the Perdew-Burke-Ernzerhof functional[92] under the generalized gradient approximation. Furthermore, the electron-ion interactions are characterized by the projector-augmented wave pseudopotentials[93]. In the calculations of wave functions, plane waves have an maximum energy cutoff of 500 eV. The vacuum distances between two neighboring nanoribbons along the z-axis and y-axis are, respectively, set to be at least 15 Å and 12 Å. The first Brillouin zone is sampled in a Gamma scheme along the periodic direction by $21 \times 1 \times 1$ k points for all structure relaxations, and by $200 \times 1 \times 1$ for further studies on electronic properties. Setting the Hellmann-Feynman forces weaker than 0.01 eV/Å and the total energy difference of $\Delta E_t < 10^{-5}$ eV are to determine the convergence criterion for structure relaxation. Regarding Gaussian smearing, the width of 0.05 eV is taken for the density of states (DOS).

References

1. Tuinstra, F. & Koenig, J. L. Raman spectrum of graphite. *J. Chem. Phys.* **53**, 1126–1130, doi:10.1063/1.1674108 (1970).
2. Huang, C. S., Lin, M. F. & Chuu, D. S. Collective excitations in graphite layers. *Solid State Commun.* **103**, 603–606, doi:10.1016/S0038-1098(97)00276-7 (1997).
3. Novoselov, K. S. *et al.* Electric field effect in atomically thin carbon films. *Science* **306**, 666–669, doi:10.1126/science.1102896 (2004).
4. Novoselov, K. S. *et al.* Two-dimensional gas of massless Dirac fermions in graphene. *Nature* **438**, 197–200, doi:10.1038/nature04233 (2005).
5. Son, Y. W., Cohen, M. L. & Louie, S. G. Half-metallic graphene nanoribbons. *Nature* **444**, 347–349, doi:10.1038/nature05180 (2006).
6. Li, X. L., Wang, X. R., Zhang, L., Lee, S. & Dai, H. Chemically derived, ultrasmooth graphene nanoribbon semiconductors. *Science* **319**, 1229–1232, doi:10.1126/science.1150878 (2008).
7. Iijima, S. Helical microtubules of graphitic carbon. *Nature* **354**, 56–58, doi:10.1038/354056a0 (1991).
8. Iijima, S. & Ichihashi, T. Single-shell carbon nanotubes of 1-nm diameter. *Nature* **363**, 603–605, doi:10.1038/363603a0 (1993).
9. Datta, S. S., Strachan, D. R., Khamis, S. M. & Johnson, A. C. Crystallographic etching of few-layer graphene. *Nano Lett.* **8**, 1912–1915, doi:10.1021/nl080583r (2008).
10. Ci, L. *et al.* Controlled nanocutting of graphene. *Nano Res* **1**, 116–122, doi:10.1007/s12274-008-8020-9 (2008).
11. McAllister, M. J. *et al.* Single sheet functionalized graphene by oxidation and thermal expansion of graphite. *Chem. Mater.* **19**, 4396–4404, doi:10.1021/cm0630800 (2007).
12. Fujii, S. & Enoki, T. Cutting of oxidized graphene into nanosized pieces. *J. Am. Chem. Soc.* **132**, 10034–10041, doi:10.1021/ja101265r (2010).
13. Han, M. Y., Özyilmaz, B., Zhang, Y. & Kim, P. Energy band-gap engineering of graphene nanoribbons. *Phys. Rev. Lett.* **98**, 206805, doi:10.1103/PhysRevLett.98.206805 (2007).
14. Chen, Z., Lin, Y. M., Rooks, M. J. & Avouris, P. Graphene nano-ribbon electronics. *Physica E: Low-dimensional Systems and Nanostructures* **40**, 228–232, doi:10.1016/j.physe.2007.06.020 (2007).
15. Wang, X. *et al.* Room-temperature all-semiconducting sub-10-nm graphene nanoribbon field-effect transistors. *Phys. Rev. Lett.* **100**, 206803, doi:10.1103/PhysRevLett.100.206803 (2008).
16. Ruffieux, P. *et al.* Electronic structure of atomically precise graphene nanoribbons. *Acs Nano* **6**, 6930–6935, doi:10.1021/nn3021376 (2012).
17. Huang, H. *et al.* Spatially resolved electronic structures of atomically precise armchair graphene nanoribbons. *Sci. Rep.* **2**, 983, doi:10.1038/srep00983 (2012).
18. Kosynkin, D. V. *et al.* Longitudinal unzipping of carbon nanotubes to form graphene nanoribbons. *Nature* **458**, 872–876, doi:10.1038/nature07872 (2009).

19. Cataldo, F. *et al*. Graphene nanoribbons produced by the oxidative unzipping of single-wall carbon nanotubes. *Carbon* **48**, 2596–2602, doi:10.1016/j.carbon.2010.03.063 (2010).
20. Kumar, P., Panchakarla, L. S. & Rao, C. N. R. Laser-induced unzipping of carbon nanotubes to yield graphene nanoribbons. *Nanoscale* **3**, 2127–2129, doi:10.1039/c1nr10137d (2011).
21. Elías, A. L. *et al*. Longitudinal cutting of pure and doped carbon nanotubes to form graphitic nanoribbons using metal clusters as nanoscalpels. *Nano Lett.* **10**, 366–372, doi:10.1021/nl901631z (2009).
22. Parashar, U. K., Bhandari, S., Srivastava, R. K., Jariwala, D. & Srivastava, A. Single step synthesis of graphene nanoribbons by catalyst particle size dependent cutting of multiwalled carbon nanotubes. *Nanoscale* **3**, 3876–3882, doi:10.1039/c1nr10483g (2011).
23. Jiao, L., Zhang, L., Wang, X., Diankov, G. & Dai, H. Narrow graphene nanoribbons from carbon nanotubes. *Nature* **458**, 877–880, doi:10.1038/nature07919 (2009).
24. Jiao, L., Zhang, L., Ding, L., Liu, J. & Dai, H. Aligned graphene nanoribbons and crossbars from unzipped carbon nanotubes. *Nano Res* **3**, 387–394, doi:10.1007/s12274-010-1043-z (2010).
25. Talyzin, A. V. *et al*. Hydrogenation, purification, and unzipping of carbon nanotubes by reaction with molecular hydrogen: Road to graphane nanoribbons. *ACS Nano* **5**, 5132–5140, doi:10.1021/nn201224k (2011).
26. Paiva, M. C. *et al*. Unzipping of functionalized multiwall carbon nanotubes induced by STM. *Nano Lett.* **10**, 1764–1768, doi:10.1021/nl100240n (2010).
27. Kim, K., Sussman, A. & Zettl, A. Graphene nanoribbons obtained by electrically unwrapping carbon nanotubes. *ACS Nano* **4**, 3–6, doi:10.1021/nn901782g (2010).
28. Cano Márquez, A. G. *et al*. Ex-mwnts: Graphene sheets and ribbons produced by lithium intercalation and exfoliation of carbon nanotubes. *Nano Lett.* **9**, 1527–1533, doi:10.1021/nl803585s (2009).
29. Shinde, D. B., Debgupta, J., Kushwaha, A., Aslam, M. & Pillai, V. K. Electrochemical unzipping of multi-walled carbon nanotubes for facile synthesis of high-quality graphene nanoribbons. *J. Am. Chem. Soc.* **133**, 4168–4171, doi:10.1021/ja1101739 (2011).
30. Campos Delgado, J. *et al*. Bulk production of a new form of sp_2 carbon: Crystalline graphene nanoribbons. *Nano Lett.* **8**, 2773–2778, doi:10.1021/nl801316d (2008).
31. Yang, X. *et al*. Two-dimensional graphene nanoribbons. *J. Am. Chem. Soc.* **130**, 4216–4217, doi:10.1021/ja710234t (2008).
32. Chung, H. C., Chang, C. P., Lin, C. Y. & Lin, M. F. Electronic and optical properties of graphene nanoribbons in external fields. *Phys. Chem. Chem. Phys.* **18**, 7573–7616, doi:10.1039/c5cp06533j (2016).
33. Kim, W. Y. & Kim, K. S. Prediction of very large values of magnetoresistance in a graphene nanoribbon device. *Nat. Nanotechnol* **3**, 408–412, doi:10.1038/nnano.2008.163 (2008).
34. Yang, L., Cohen, M. L. & Louie, S. G. Excitonic effects in the optical spectra of graphene nanoribbons. *Nano Lett.* **7**, 3112–3115, doi:10.1021/nl0716404 (2007).
35. Lin, M. F. & Shyu, F. L. Optical properties of nanographite ribbons. *J. Phys. Soc. Jpn.* **69**, 3529–3532, doi:10.1143/JPSJ.69.3529 (2000).
36. Li, Z., Qian, H., Wu, J., Gu, B. L. & Duan, W. Role of symmetry in the transport properties of graphene nanoribbons under bias. *Phys. Rev. Lett.* **100**, 206802, doi:10.1103/PhysRevLett.100.206802 (2008).
37. Basu, D., Gilbert, M. J., Register, L. F., Banerjee, S. K. & MacDonald, A. H. Effect of edge roughness on electronic transport in graphene nanoribbon channel metal-oxide-semiconductor field-effect transistors. *Appl. Phys. Lett.* **92**, 042114, doi:10.1063/1.2839330 (2008).
38. Son, Y. W., Cohen, M. L. & Louie, S. G. Energy gaps in graphene nanoribbons. *Phys. Rev. Lett.* **97**, 216803, doi:10.1103/PhysRevLett.97.216803 (2006).
39. Barone, V., Hod, O. & Scuseria, G. E. Electronic structure and stability of semiconducting graphene nanoribbons. *Nano Lett.* **6**, 2748–2754, doi:10.1021/nl0617033 (2006).
40. Ritter, K. A. & Lyding, J. W. The influence of edge structure on the electronic properties of graphene quantum dots and nanoribbons. *Nat. Mater.* **8**, 235–242, doi:10.1038/nmat2378 (2009).
41. Chang, S. L., Lin, S. Y., Lin, S. K., Lee, C. H. & Lin, M. F. Geometric and electronic properties of edge-decorated graphene nanoribbons. *Sci. Rep.* **4**, 6038, doi:10.1038/srep06038 (2014).
42. Lin, Y. T., Chung, H. C., Yang, P. H., Lin, S. Y. & Lin, M. F. Adatom bond-induced geometric and electronic properties of passivated armchair graphene nanoribbons. *Phys. Chem. Chem. Phys.* **17**, 16545–16552, doi:10.1039/c5cp02226f (2015).
43. Johnson, J. L., Behnam, A., Pearton, S. J. & Ural, A. Hydrogen sensing using Pd-functionalized multi-layer graphene nanoribbon networks. *Adv. Mater.* **22**, 4877–4880, doi:10.1002/adma.201001798 (2010).
44. Lin, J. *et al*. Graphene nanoribbon and nanostructured SnO_2 composite anodes for lithium ion batteries. *ACS Nano* **7**, 6001–6006, doi:10.1021/nn4016899 (2013).
45. Huang, Y. C., Chang, C. P. & Lin, M. F. Magnetoabsorption spectra of bilayer graphene ribbons with bernal stacking. *Phys. Rev. B* **78**, 115422, doi:10.1103/PhysRevB.78.115422 (2008).
46. Sadeghi, H., Ahmadi, M. T., Mousavi, S. M., Ismail, R. & Ghadiry, M. H. Channel conductance of ABA stacking trilayer graphene nanoribbon field-effect transistor. *Mod. Phys. Lett. B* **26**, 1250047, doi:10.1142/S0217984912500479 (2012).
47. Lin, C. Y., Chen, S. C., Wu, J. Y. & Lin, M. F. Curvature effects on magnetoelectronic properties of nanographene ribbons. *J. Phys. Soc. Jpn.* **81**, 064719, doi:10.1143/JPSJ.81.064719 (2012).
48. Chang, S. L., Wu, B. R., Yang, P. H. & Lin, M. F. Curvature effects on electronic properties of armchair graphene nanoribbons without passivation. *Phys. Chem. Chem. Phys.* **14**, 16409–16414, doi:10.1039/c2cp42721d (2012).
49. Chang, C. P., Wu, B. R., Chen, R. B. & Lin, M. F. Deformation effect on electronic and optical properties of nanographite ribbons. *J. Appl. Phys.* **101**, 063506, doi:10.1063/1.2710761 (2007).
50. Lin, S. Y., Chang, S. L., Shyu, F. L., Lu, J. M. & Lin, M. F. Feature-rich electronic properties in graphene ripples. *Carbon* **86**, 207–216, doi:10.1016/j.carbon.2014.12.068 (2015).
51. Chang, C. P. *et al*. Electronic and optical properties of a nanographite ribbon in an electric field. *Carbon* **44**, 508–515, doi:10.1016/j.carbon.2005.08.009 (2006).
52. Kan, E. J., Li, Z., Yang, J. & Hou, J. Will zigzag graphene nanoribbon turn to half metal under electric field? *Appl. Phys. Lett.* **91**, 243116, doi:10.1063/1.2821112 (2007).
53. Raza, H. & Kan, E. C. Armchair graphene nanoribbons: Electronic structure and electric-field modulation. *Phys. Rev. B* **77**, 245434, doi:10.1103/PhysRevB.77.245434 (2008).
54. Huang, Y. C., Chang, C. P. & Lin, M. F. Magnetic and quantum confinement effects on electronic and optical properties of graphene ribbons. *Nanotechnology* **18**, 495401, doi:10.1088/0957-4484/18/49/495401 (2007).
55. Liu, J., Wright, A. R., Zhang, C. & Ma, Z. Strong terahertz conductance of graphene nanoribbons under a magnetic field. *Appl. Phys. Lett.* **93**, 041106, doi:10.1063/1.2964093 (2008).
56. Obradovic, B. *et al*. Analysis of graphene nanoribbons as a channel material for field-effect transistors. *Appl. Phys. Lett.* **88**, 142102, doi:10.1063/1.2191420 (2006).
57. Saffarzadeh, A. & Farghadan, R. A spin-filter device based on armchair graphene nanoribbons. *Appl. Phys. Lett.* **98**, 023106, doi:10.1063/1.3537965 (2011).
58. Tapasztó, L., Dobrik, G., Lambin, P. & Biró, L. P. Tailoring the atomic structure of graphene nanoribbons by scanning tunnelling microscope lithography. *Nat. Nanotechnol* **3**, 397–401, doi:10.1038/nnano.2008.149 (2008).
59. Söde, H. *et al*. Electronic band dispersion of graphene nanoribbons via Fourier-transformed scanning tunneling spectroscopy. *Phys. Rev. B* **91**, 045429, doi:10.1103/PhysRevB.91.045429 (2015).

60. Chen, Y. C. *et al.* Tuning the band gap of graphene nanoribbons synthesized from molecular precursors. *ACS Nano* **7**, 6123–6128, doi:10.1021/nn401948e (2013).
61. Mao, Y. L., Hao, W. P., Wei, X. L., Yuan, J. & Zhong, J. X. Edge-adsorption of potassium adatoms on graphene nanoribbon: A first principle study. *Appl. Surf. Sci.* **280**, 698–704, doi:10.1016/j.apsusc.2013.05.045 (2013).
62. Wang, Y., Cao, C. & Cheng, H. P. Metal-terminated graphene nanoribbons. *Phys. Rev. B* **82**, 205429, doi:10.1103/PhysRevB.82.205429 (2010).
63. Cao, C., Wang, Y., Cheng, H. P. & Jiang, J. Z. Perfect spin-filtering and giant magnetoresistance with Fe-terminated graphene nanoribbon. *Appl. Phys. Lett.* **99**, 073110, doi:10.1063/1.3626596 (2011).
64. Wang, Z. Y., Xiao, J. R. & Li, M. Adsorption of transition metal atoms (Co and Ni) on zigzag graphene nanoribbon. *Appl. Phys. A* **110**, 235–239, doi:10.1007/s00339-012-7119-8 (2013).
65. Da Rocha, C. G., Clayborne, P. A., Koskinen, P. & Häkkinen, H. Optical and electronic properties of graphene nanoribbons upon adsorption of ligand-protected aluminum clusters. *Phys. Chem. Chem. Phys.* **16**, 3558–3565, doi:10.1039/c3cp53780c (2014).
66. Uthaisar, C., Barone, V. & Peralta, J. E. Lithium adsorption on zigzag graphene nanoribbons. *J. Appl. Phys.* **106**, 113715, doi:10.1063/1.3265431 (2009).
67. Lee, Y. L., Kim, S., Park, C., Ihm, J. & Son, Y. W. Controlling half-metallicity of graphene nanoribbons by using a ferroelectric polymer. *ACS Nano* **4**, 1345–1350, doi:10.1021/nn9019064 (2010).
68. Wong, B. M., Simon, H. Y. & O'Bryan, G. Reversible, opto-mechanically induced spin-switching in a nanoribbon-spiropyran hybrid material. *Nanoscale* **4**, 1321–1327, doi:10.1039/c2nr11543c (2012).
69. Virojanadara, C., Watcharinyanon, S., Zakharov, A. A. & Johansson, L. I. Epitaxial graphene on 6H-SiC and Li intercalation. *Phys. Rev. B* **82**, 205402, doi:10.1103/PhysRevB.82.205402 (2010).
70. Cao, C., Wu, M., Jiang, J. & Cheng, H. P. Transition metal adatom and dimer adsorbed on graphene: Induced magnetization and electronic structures. *Phys. Rev. B* **81**, 205424, doi:10.1103/PhysRevB.81.205424 (2010).
71. Lin, M. C. *et al.* An ultrafast rechargeable aluminium-ion battery. *Nature* **520**, 324–328, doi:10.1038/nature14340 (2015).
72. Rani, J. V., Kanakaiah, V., Dadmal, T., Rao, M. S. & Bhavanarushi, S. Fluorinated natural graphite cathode for rechargeable ionic liquid based aluminum–ion battery. *J. Electrochem. Soc.* **160**, 1781–1784, doi:10.1149/2.072310jes (2013).
73. Paek, S. M., Yoo, E. J. & Honma, I. Enhanced cyclic performance and lithium storage capacity of SnO_2/graphene nanoporous electrodes with three-dimensionally delaminated flexible structure. *Nano Lett.* **9**, 72–75, doi:10.1021/nl802484w (2008).
74. Wang, G., Shen, X., Yao, J. & Park, J. Graphene nanosheets for enhanced lithium storage in lithium ion batteries. *Carbon* **47**, 2049–2053, doi:10.1016/j.carbon.2009.03.053 (2009).
75. Sugawara, K., Sato, T., Souma, S., Takahashi, T. & Suematsu, H. Fermi surface and edge-localized states in graphite studied by high-resolution angle-resolved photoemission spectroscopy. *Phys. Rev. B* **73**, 045124, doi:10.1103/PhysRevB.73.045124 (2006).
76. Grüneis, A. *et al.* Electron-electron correlation in graphite: A combined angle-resolved photoemission and first-principles study. *Phys. Rev. Lett.* **100**, 037601, doi:10.1103/PhysRevLett.100.037601 (2008).
77. Ohta, T. *et al.* Interlayer interaction and electronic screening in multilayer graphene investigated with angle-resolved photoemission spectroscopy. *Phys. Rev. Lett.* **98**, 206802, doi:10.1103/PhysRevLett.98.206802 (2007).
78. Siegel, D. A., Regan, W., Fedorov, A. V., Zettl, A. & Lanzara, A. Charge-carrier screening in single-layer graphene. *Phys. Rev. Lett.* **110**, 146802, doi:10.1103/PhysRevLett.110.146802 (2013).
79. Bostwick, A., Ohta, T., Seyller, T., Horn, K. & Rotenberg, E. Quasiparticle dynamics in graphene. *Nat. Phys* **3**, 36–40, doi:10.1038/nphys477 (2007).
80. Ohta, T., Bostwick, A., Seyller, T., Horn, K. & Rotenberg, E. Controlling the electronic structure of bilayer graphene. *Science* **313**, 951–954, doi:10.1126/science.1130681 (2006).
81. Coletti, C. *et al.* Revealing the electronic band structure of trilayer graphene on SiC: An angle-resolved photoemission study. *Phys. Rev. B* **88**, 155439, doi:10.1103/PhysRevB.88.155439 (2013).
82. Zhou, S. Y., Siegel, D. A., Fedorov, A. V. & Lanzara, A. Metal to insulator transition in epitaxial graphene induced by molecular doping. *Phys. Rev. Lett.* **101**, 086402, doi:10.1103/PhysRevLett.101.086402 (2008).
83. Schulte, K., Vinogradov, N. A., Ng, M. L., Mårtensson, N. & Preobrajenski, A. B. Bandgap formation in graphene on Ir(111) through oxidation. *Appl. Surf. Sci.* **267**, 74–76, doi:10.1016/j.apsusc.2012.07.122 (2013).
84. Klusek, Z. Investigations of splitting of the π bands in graphite by scanning tunneling spectroscopy. *Appl. Surf. Sci.* **151**, 251–261 (1999).
85. Li, G. H., Luican, A. & Andrei, E. Y. Scanning tunneling spectroscopy of graphene on graphite. *Phys. Rev. Lett.* **102**, 176804, doi:10.1103/PhysRevLett.102.176804 (2009).
86. Luican, A. *et al.* Single-layer behavior and its breakdown in twisted graphene layers. *Phys. Rev. Lett.* **106**, 126802, doi:10.1103/PhysRevLett.106.126802 (2011).
87. Li, G. H. *et al.* Observation of Van Hove singularities in twisted graphene layers. *Nat. Phys* **6**, 109–113 (2010).
88. Cherkez, V., De Laissardiere, G. T., Mallet, P. & Veuillen, J. Y. Van Hove singularities in doped twisted graphene bilayers studied by scanning tunneling spectroscopy. *Phys. Rev. B* **91**, 155428, doi:10.1103/PhysRevB.91.155428 (2015).
89. Wilder, J. W. G., Venema, L. C., Rinzler, A. G., Smalley, R. E. & Dekker, C. Electronic structure of atomically resolved carbon nanotubes. *Nature* **391**, 59–62, doi:10.1038/34139 (1998).
90. Odom, T. W., Huang, J. L., Kim, P. & Lieber, C. M. Atomic structure and electronic properties of single-walled carbon nanotubes. *Nature* **391**, 62–64, doi:10.1038/34145 (1998).
91. Kresse, G. & Furthmüller, J. Efficient iterative schemes for ab initio total-energy calculations using a plane-wave basis set. *Phys. Rev. B* **54**, 11169–11186, doi:10.1103/PhysRevB.54.11169 (1996).
92. Perdew, J. P., Burke, K. & Ernzerhof, M. Generalized gradient approximation made simple. *Phys. Rev. Lett.* **77**, 3865–3868, doi:10.1103/PhysRevLett.77.3865 (1996).
93. Blöchl, P. E. Projector augmented-wave method. *Phys. Rev. B* **50**, 17953–17979, doi:10.1103/PhysRevB.50.17953 (1994).

Acknowledgements

This work was supported by the Nation Science Council of Taiwan (Grant No. NSC 105-2112-M-006-002-MY3). We also thank the National Center for High-performance Computing (NCHC) for computer facilities.

Author Contributions

Y.T.L. did numerical calculations under the guidance of M.F.L. and Y.H.C. and S.Y.L. contributed to the writing of the manuscript.

Additional Information

Competing Interests: The authors declare that they have no competing interests.